

# Computational Screening of $p$ -Type Transparent Conducting Oxides Using the Optical Absorption Spectra and Oxygen-Vacancy Formation Energies

Yu Kumagai \**Institute for Materials Research, Tohoku University, 2-1-1 Katahira, Aoba-ku, Sendai, 980-8577, Japan*

(Received 11 January 2023; revised 12 February 2023; accepted 15 February 2023; published 20 March 2023)

Although  $n$ -type transparent conducting oxides (TCOs) with visible-light transparency and electric conductivity have been used in industry for decades, their  $p$ -type counterparts have not been commercialized. To search for promising  $p$ -type TCOs, computational screening was applied by several research groups in the last decade. However, screening of a wide material space is mainly based on the approximated physical quantities, such as underestimated band gaps, and band-alignment techniques. In particular, it is unlikely that band alignments can predict the dopability of a wide range of insulators because they do not include information about the chemical potentials of the constituent elements. In this study, we use optical absorption spectra calculated with dielectric dependent hybrid functionals and the formation energies of oxygen vacancies as screening parameters. Oxygen vacancies are known to act as hole killers when seeking  $p$ -type TCOs, and indeed, only 156 out of the 845 oxides are found to have benign oxygen vacancies for  $p$ -type doping. As a result, we identify six potential  $p$ -type TCOs from 845 oxides:  $\text{Na}_3\text{AgO}_2$ ,  $\text{Rb}_2\text{Pb}_2\text{O}_3$ ,  $\text{Cs}_2\text{Pb}_2\text{O}_3$ ,  $\text{CsCuO}$ ,  $\text{K}_2\text{Pb}_2\text{O}_3$ , and  $\text{B}_6\text{O}$ .  $\text{Na}_3\text{AgO}_2$ ,  $\text{Rb}_2\text{Pb}_2\text{O}_3$ , and  $\text{Cs}_2\text{Pb}_2\text{O}_3$  are identified as potential  $p$ -type TCOs, while  $\text{CsCuO}$ ,  $\text{K}_2\text{Pb}_2\text{O}_3$ , and  $\text{B}_6\text{O}$  were previously proposed. By analyzing the electronic structures and point-defect properties of  $\text{Na}_3\text{AgO}_2$ ,  $\text{CsCuO}$ , and  $\text{K}_2\text{Pb}_2\text{O}_3$  in detail, we find that they show  $p$ -type conductivity, even without external doping, which validates the use of the formation energies of oxygen vacancies as descriptors of the  $p$ -type dopability of oxides.

DOI: [10.1103/PhysRevApplied.19.034063](https://doi.org/10.1103/PhysRevApplied.19.034063)

## I. INTRODUCTION

Transparent conductors (TCs) that show both visible-light transparency and electric conductivity can be used for various applications, such as transparent thin-film transistors, touch-panel displays, and photovoltaic cells [1,2]. Because of the incompatibility between transparency and electric conductivity, only a limited number of TCs have been discovered. After many years of research, Sn-doped  $\text{In}_2\text{O}_3$  has become the representative  $n$ -type transparent conducting oxide (TCO), and it has been commercially used for decades [3]. Amorphous indium gallium zinc oxide was also recently used because of its high mobility at low processing temperatures, relatively low fabrication cost, and good transparency [4].

The performance of  $p$ -type TCOs is not sufficiently high for them to be commercialized. Oxides are a promising class of  $p$ -type TCs because they tend to have relatively wide band gaps and can be easily synthesized under atmospheric conditions [5,6]. Furthermore, the heterojunction between oxides is desirable to suppress oxygen-related defect states at the interface. The problem is that  $p$ -type doping in oxides is usually difficult because the energy levels of the O  $2p$  bands are too deep to introduce hole

carriers. In 1997, Kawazoe *et al.* proposed that oxides were  $p$ -type dopable when the valence band was pushed up by hybridizing the O  $2p$  bands with cationic orbitals, the levels of which were comparable with those of the O  $2p$  orbitals [7]. They demonstrated the strategy with  $\text{CuAlO}_2$ , in which the Cu  $3d$  orbitals hybridized with the O  $2p$  orbitals.

After the discovery of  $\text{CuAlO}_2$ , several candidates for  $p$ -type TCOs were proposed [5], and their computational screening has flourished in the last decade [8–15]. For example, Hautier *et al.* [8] reported extensive screening of  $p$ -type TCOs from thousands of oxides in 2013. In their study, the candidates were initially screened based on the hole effective masses and band gaps calculated using the Perdew-Burke-Ernzerhof (PBE) generalized-gradient approximation [16]. For the screened oxides, they calculated more accurate band gaps with the one-shot  $GW$  approximation ( $G_0W_0$ ) [17] and vacancy-formation energies with PBE. Similar high-throughput first-principles screening was also performed for compounds other than oxides, such as phosphides and sulfides [10,11].

$P$ -type TCOs should be screened in view of their optical transparency and electric conductivity. In computational studies, transparency is mostly approximated by the minimum direct band gap in the reciprocal space. However, the optical gaps are much larger than those when the

\*yukumagai@tohoku.ac.jp

band-edge transitions are dipole prohibited. In fact, the minimum direct transitions in many TCOs are dipole forbidden, including in  $\text{In}_2\text{O}_3$  [18],  $\text{SnO}_2$  [19], and  $\text{CuAlO}_2$  [20]. It is therefore more desirable to use the optical absorption spectrum as a screening criterion.

The band gaps used for initial screening are mostly calculated using semilocal functionals, such as the PBE functional [16], which usually greatly underestimates the band gaps. The problem is not underestimation but that the trend is not consistent. For example, the PBE band gap of ZnO is 0.73 eV, as reported in the Materials Project [21], which is only 22% of the experimental value of 3.3 eV [22]. In contrast, the PBE band gap of monoclinic  $\text{HfO}_2$  is 4.0 eV, which is 70% of the experimental band gap of 5.7 eV [23]. Such large uncertainty will increase the numbers of false positives and false negatives in the screened candidates and excluded materials, respectively.

The electric conductivity,  $\sigma$ , can be expressed as

$$\sigma = en\mu = e^2 n \frac{\tau}{m^*}, \quad (1)$$

where  $e$  is the elementary charge,  $\mu$  is the mobility ( $= e\tau/m^*$ ),  $n$  is the carrier concentration,  $\tau$  is the average diffusion time, and  $m^*$  is the effective mass [24].  $\tau$  is generally difficult to calculate from first principles. Although different computational methods were proposed recently [25], it is still not easy to perform high-throughput calculations. Thus, it is not explicitly considered in computational screening. Conversely,  $m^*$  is easily evaluated from the band structure or density of states (DOS). All of the best  $n$ -type TCOs show very low electron effective masses, which legitimates the use of the effective mass as a criterion [8].

In addition to  $\mu$ , the feasibility of  $p$ -type doping that is related to the carrier concentration is a key factor, because it is not easily realized in oxides, as mentioned above. The  $p$ -type doping necessitates acceptor-type native defects and/or dopants with small formation energies. In addition, the donor-type defects that annihilate holes, or so-called “hole killers,” should be suppressed and have larger formation energies at the Fermi level located near the valence-band maximum (VBM) [26]. Although the importance of the defect properties was emphasized in previous screening studies [8,9,14], it is generally cumbersome and computationally demanding to calculate the energies of point defects from first principles. Therefore, in the initial screening phase, the dopability is determined using more easily calculated band alignments. Some studies use the branch-point energies [11,14], but their prediction capability is questionable [9,11]. Yim *et al.* proposed to use the hydrogen-impurity energy as a descriptor, which is shown to successfully distinguish established  $p$ - and  $n$ -type TCOs [9]. However, this technique is also considered an alternative band-alignment technique because it determines the position of the VBM with respect to the reference level at

the constant H chemical potential (e.g., the  $\text{H}_2$  molecule energy).

The chemical potentials of the constituent elements are controllable as long as the host material is stable with respect to the competing phases, and they are directly related to the defect-formation energies. For example, when the O chemical potential is decreased by 1 eV, the concentration of oxygen vacancies ( $V_{\text{O}}$ ) is increased by a factor of  $10^5$  at a typical sintering temperature of 1273 K. However, the aforementioned alignment techniques do not, in principle, include information about the chemical potentials, unfortunately. Therefore, it is desirable to use defect-formation energies, even in the initial screening, while taking into account the chemical potentials. Based on previous theoretical studies on point defects in oxides such as ZnO [26],  $\text{In}_2\text{O}_3$  [27],  $\text{SnO}_2$  [27],  $\text{BaTiO}_3$  [28], and  $\text{SrTiO}_3$  [29],  $V_{\text{O}}$  are typical native defects and tend to act as the main hole killers.

Here, we screen 845 oxides for potential  $p$ -type TCOs using the physical properties directly linked to the transparency (optical absorption spectra) and conductivity (oxygen-vacancy formation energies and effective masses). The band structures, effective masses, and optical absorption spectra are calculated, while we use our previous high-throughput calculations of  $V_{\text{O}}$  [30] for screening of the  $p$ -type dopability. For the first-principles calculations, we use dielectric dependent (DD) hybrid functionals, which can accurately predict band gaps [31].

The screening identifies six potential  $p$ -type TCOs:  $\text{Na}_3\text{AgO}_2$ ,  $\text{Rb}_2\text{Pb}_2\text{O}_3$ ,  $\text{Cs}_2\text{Pb}_2\text{O}_3$ ,  $\text{CsCuO}$ ,  $\text{K}_2\text{Pb}_2\text{O}_3$ , and  $\text{B}_6\text{O}$ .  $\text{Na}_3\text{AgO}_2$  is identified to be a potential  $p$ -type TCO, while  $\text{CsCuO}$  [9],  $\text{K}_2\text{Pb}_2\text{O}_3$  [8], and  $\text{B}_6\text{O}$  [8] were previously identified.  $\text{Rb}_2\text{Pb}_2\text{O}_3$  and  $\text{Cs}_2\text{Pb}_2\text{O}_3$  are also identified as potential TCOs, although they are related compounds to  $\text{K}_2\text{Pb}_2\text{O}_3$ . For  $\text{Na}_3\text{AgO}_2$ ,  $\text{CsCuO}$ , and  $\text{K}_2\text{Pb}_2\text{O}_3$ , we calculate not only the vacancies, but also the antisites and interstitials using the DD hybrid functionals. We find that they are indeed  $p$ -type semiconductors, even without external doping. However, it is found that  $\text{Na}_3\text{AgO}_2$  and  $\text{CsCuO}$  exhibit one-dimensional (1D) or small polaronic states, which would lead to anisotropic or small conductivity, respectively. On the other hand,  $\text{K}_2\text{Pb}_2\text{O}_3$  acts as a  $p$ -type semiconductor with moderate carrier concentration, and it can be enhanced via Na doping.

## II. COMPUTATIONAL METHODS

### A. Computational settings of first-principles calculations

The first-principles calculations are performed using the projector-augmented-wave (PAW) method [32,33] implemented in the Vienna *ab initio* simulation package (VASP) [34]. We use the same PAW data sets as those used in our previous study [30]. To use the oxygen-vacancy formation energies ( $E_f[V_{\text{O}}]$ ) calculated in our previous study [30], we

target 845 oxides, for which all of the inequivalent oxygen vacancies are successfully calculated. In these calculations, three charge states (0, +1, and +2) are considered for oxygen vacancies. The unit cells relaxed with the PBEsol functional [35] are used for the high-throughput calculations in this study.

The calculations of the band structures and optical absorption spectra are performed using the DD hybrid functionals [31], in which the exchange-correlation (XC) interactions are evaluated by

$$v_{\text{XC}}(\mathbf{r}, \mathbf{r}') = av_X^{\text{NL}}(\mathbf{r}, \mathbf{r}') + (1 - a)v_X^l(\mathbf{r}) + v_C^l(\mathbf{r}), \quad (2)$$

where  $v_X^{\text{NL}}(\mathbf{r}, \mathbf{r}')$  and  $v_X^l(\mathbf{r})$  are the nonlocal and (semi)local exchange potentials, respectively.  $v_C^l(\mathbf{r})$  is a correlation potential estimated from a (semi)local potential. The mixing parameter for an exchange potential is determined by  $a = \varepsilon_{\text{ele}}^{-1}$ , where  $\varepsilon_{\text{ele}}$  is the spherically averaged ion-clamped dielectric constant. The  $\varepsilon_{\text{ele}}$  values are also taken from our previous study [30], in which the dielectric constants are calculated using the PBEsol functional with Hubbard  $U$  corrections [36] for the Cu and Zn  $3d$  orbitals and Ce  $4f$  orbitals with  $U_{\text{eff}} = 5$  eV [PBEsol(+ $U$ )]. We use PBEsol [35] for  $v_X^l(\mathbf{r})$  and  $v_C^l(\mathbf{r})$  in Eq. (2).

For the band-structure calculations of the 845 oxides and some screened oxides, the  $k$ -point sampling densities are set to 2.5 and 3.5  $\text{\AA}^{-3}$ , and the band paths are determined using seeK-path [37] with mesh distances of 0.025 and 0.015  $\text{\AA}^{-1}$ , respectively. When calculating the dielectric functions, the  $k$ -point density is doubled along all of the reciprocal axes and the  $k$ -point meshes are centered at the  $\Gamma$  point for sampling the special points at the zone boundaries. To reduce the computational time, the  $k$ -point sampling for the exact exchange potential is reduced by half in all of the directions.

To calculate the optical absorption spectra, we first obtain the imaginary parts of the dielectric functions,  $\epsilon_2$ . The real parts,  $\epsilon_1$ , are then calculated using the Kramers-Kronig transformation with a complex shift of 0.01 eV. We

next estimate their spherical averages,  $\bar{\epsilon}_1$  and  $\bar{\epsilon}_2$ , and the optical absorption spectra:

$$\alpha = \frac{4\pi}{\lambda} \sqrt{\frac{1}{2} \left( -\bar{\epsilon}_1 + \sqrt{(\bar{\epsilon}_1^2 + \bar{\epsilon}_2^2)} \right)}, \quad (3)$$

where  $\lambda$  is the wavelength [38]. When strong absorption is allowed near the band edges, the absorption spectrum shows a steep increase to  $>10^4 \text{ cm}^{-1}$  just above the band gap. Therefore, we define the optical gaps as the energies at which the absorption spectra first reach  $10^4 \text{ cm}^{-1}$ .

The band-averaged effective-mass tensors and DOS are also evaluated based on the calculations of the dielectric functions. The former are calculated using BoltzTraP2 [38], where the carrier concentration and temperature are set to  $10^{16} \text{ cm}^{-3}$  and 300 K, respectively. The minima of the effective hole masses,  $m_h^*$ , are determined by diagonalizing the effective mass tensors.

All of the VASP input settings are generated using the VISE code (version 0.6.6) [39]. Automation of the first-principles calculations is performed with FireWorks [40], pymatgen [41], and Custodian [41].

## B. Modeling of point defects

For the oxygen-vacancy calculations in our previous study [30], we adopt the PBEsol functional with Hubbard  $U$  corrections with the same parameters in this study. The band-edge positions are then determined using the non-self-consistent DD hybrid functional [42].

Here, the self-consistent DD hybrid functionals are used to calculate the point defects in  $\text{Na}_3\text{AgO}_2$ ,  $\text{CsCuO}$ , and  $\text{K}_2\text{Pb}_2\text{O}_3$ . The Fock-exchange-mixing parameters are given in Table I. The lattice constants and internal coordinates in the perfect structures are fully relaxed for each mixing parameter. We construct nearly isotropic supercells by expanding the conventional unit cells. The numbers of atoms in the supercells are 96, 288, and 224 for  $\text{Na}_3\text{AgO}_2$ ,  $\text{CsCuO}$ , and  $\text{K}_2\text{Pb}_2\text{O}_3$ , respectively. The reciprocal space of  $\text{Na}_3\text{AgO}_2$  is sampled with a  $2 \times 2 \times 1$   $k$ -point grid,

TABLE I. Fundamental band gaps, optical gaps, and hole effective masses in the  $x$ ,  $y$ , and  $z$  directions calculated using the DD hybrid functionals for the screened  $p$ -type TCOs, along with those of  $\text{CuAlO}_2$  for comparison. Space groups of the crystal structures and exact exchange-mixing parameters,  $a$ , are also given. Italic numbers indicate hole masses below  $1.0m_0$ , where  $m_0$  is the free-electron rest mass. See the crystal structures in Figs. 3(a), 5(a) and 7(a) for crystal orientations.

	Space group	$a$	Fundamental band gap (eV)	Optical gap (eV)	$m_{h,x}^*(m_0)$	$m_{h,y}^*(m_0)$	$m_{h,z}^*(m_0)$
$\text{CuAlO}_2$	$R\bar{3}m$	0.207	3.91	4.46	1.80	1.80	5.59
$\text{Na}_3\text{AgO}_2$	$Ibam$	0.250	3.00	4.02	1.22	2.59	0.39
$\text{CsCuO}$	$Cmcm$	0.274	3.18	3.29	5.83	3.56	0.36
$\text{K}_2\text{Pb}_2\text{O}_3$	$I2_13$	0.193	2.43	3.00	0.33	0.33	0.33
$\text{Rb}_2\text{Pb}_2\text{O}_3$	$I2_13$	0.205	2.87	3.11	0.36	0.36	0.36
$\text{Cs}_2\text{Pb}_2\text{O}_3$	$I2_13$	0.209	2.83	3.05	0.41	0.41	0.41
$\text{B}_6\text{O}$	$R\bar{3}m$	0.172	3.02	5.12	0.58	0.58	0.58
$\text{Ba}_3\text{BaSO}_3$	$P6_3/mmc$	0.184	2.51	2.94	4.17	4.17	0.28

while CsCuO and  $K_2Pb_2O_3$  are calculated with only the  $\Gamma$  point.

We model the vacancies at all the inequivalent sites, cation antisites, and interstitials. We place the interstitial sites at the local minima of the all-electron charge densities in the perfect crystals, which are identified using scikit-image [43]. We also consider split-type vacancies and antisites at the Cu and Ag sites because the split-type Cu vacancy is known to be stable in  $Cu_2O$  [44]. To lower the initial site symmetries, atoms within 1.3 times the shortest bond length from the initial defect site are randomly displaced by up to 0.2 Å. The defect charge states are determined from the oxidation states. For example, because the oxidation states of K and Pb in  $K_2Pb_2O_3$  are 1+ and 2+, we calculate the 0 and  $-1$  charge states for the  $K_{Pb}$  antisites.

The calculations of the defect-formation energies follow the general methodology [45]. The formation energy of a point defect is given by

$$E_f[D^q] = \{E[D^q] + E_{\text{corr}}[D^q]\} - E_p + \sum_i \Delta n_i \mu_i + q(\varepsilon_{\text{VBM}} + \Delta\varepsilon_F), \quad (4)$$

where  $E[D^q]$  and  $E_p$  are the total energies of the supercell with defect  $D$  in charge state  $q$  and the perfect crystal supercell without defects, respectively.  $n_i$  is the number of  $i$ -type atoms removed ( $n_i < 0$ ) or added ( $n_i > 0$ ), and  $\mu_i$  is its chemical potential.  $\varepsilon_{\text{VBM}}$  is the energy level of the VBM, while  $\Delta\varepsilon_F$  is the Fermi level with respect to the VBM.  $E_{\text{corr}}[D^q]$  is a correction energy for the finite-size error. It is estimated using the extended Freysoldt-Neugebauer-Van de Walle scheme [46,47], which works satisfactorily for various systems [28,48–53]. Note that this correction technique is also applied to the oxygen-vacancy formation energies [30], which are used in this study. The dielectric constants are then defined as the sum of the ion-clamped and ionic dielectric constants. The former are evaluated using the DD hybrid functional in this study, while the latter are taken from our previous study using the PBEsol(+ $U$ ) functional [30]. Identification of the perturbed host states is performed according to our previously reported method [30].

We construct the chemical-potential diagrams from the total energies of the competing phases, including the impurity phases calculated using the same exact exchange-mixing parameter for each oxide. The standard state of oxygen is set to the  $O_2$  molecule. The competing phase lists are taken from the Materials Project Database (MPD) [21]. When using the oxygen-vacancy formation energies in our previous study, the chemical potentials are determined from the MPD, where the total energies are empirically corrected [30,54].

The defect and carrier concentrations are evaluated from the Boltzmann and the Fermi-Dirac distributions,

respectively. Based on their concentrations and the charge-neutrality condition, the Fermi level is finally determined (see, e.g., Ref. [49] for details). When calculating the carrier concentration at room temperature, we assume that the defects are created at the sintering temperatures, but the defect concentrations are kept fixed during quenching, while their charge states are variable.

All defect-related processes are performed with pydefect [55].

### III. RESULTS

#### A. Screening of $p$ -type TCOs

To achieve  $p$ -type doping, the native donor-type defects that compensate for the carrier holes must be suppressed. Although oxygen vacancies are ubiquitous in oxides, only positively charged oxygen vacancies act as hole killers. Because the Fermi level is close to the VBM in  $p$ -type semiconductors, the energy of the positively charged oxygen vacancy at  $\Delta\varepsilon_F = 0$  is an indicator of whether oxides are  $p$ -type dopable. In particular, when positively charged oxygen vacancies have negative  $E_f[V_O]$  at  $\Delta\varepsilon_F = 0$ , Fermi-level pinning occurs within the band gap, from which  $\Delta\varepsilon_F$  cannot be lowered, even with acceptor doping [56].

It is well known that, although considerable efforts have been made to realize  $p$ -type ZnO, only limited success has been reported [57]. Since  $E_f[V_O]$  at the O-rich condition in ZnO is close to zero, we use  $E_f[V_O] = 0$  eV at  $\Delta\varepsilon_F = 0$  as the baseline for the  $p$ -type dopability and classify the oxygen vacancies into three types:

- (1) Type 1, stable only in the neutral charge state, regardless of  $\Delta\varepsilon_F$  in the band gap (e.g.,  $V_{O1}$  and  $V_{O2}$  in Fig. 1)
- (2) Type 2, positively charged and  $E_f[V_O] > 0$  eV at  $\Delta\varepsilon_F = 0$  (e.g.,  $V_{O3}$ )
- (3) Type 3, positively charged and  $E_f[V_O] \leq 0$  eV at  $\Delta\varepsilon_F = 0$  (e.g.,  $V_{O4}$ ); the Fermi level where  $E_f[V_O]$

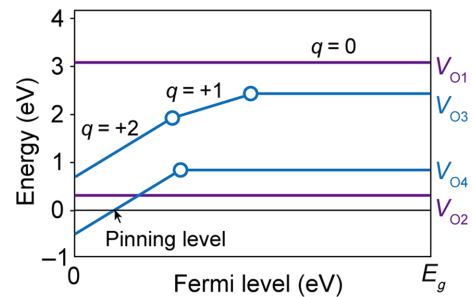


FIG. 1. Schematic representation of the formation energies of oxygen vacancies ( $V_O$ ) with charge states ( $q$ ). Transition levels are indicated by circles.

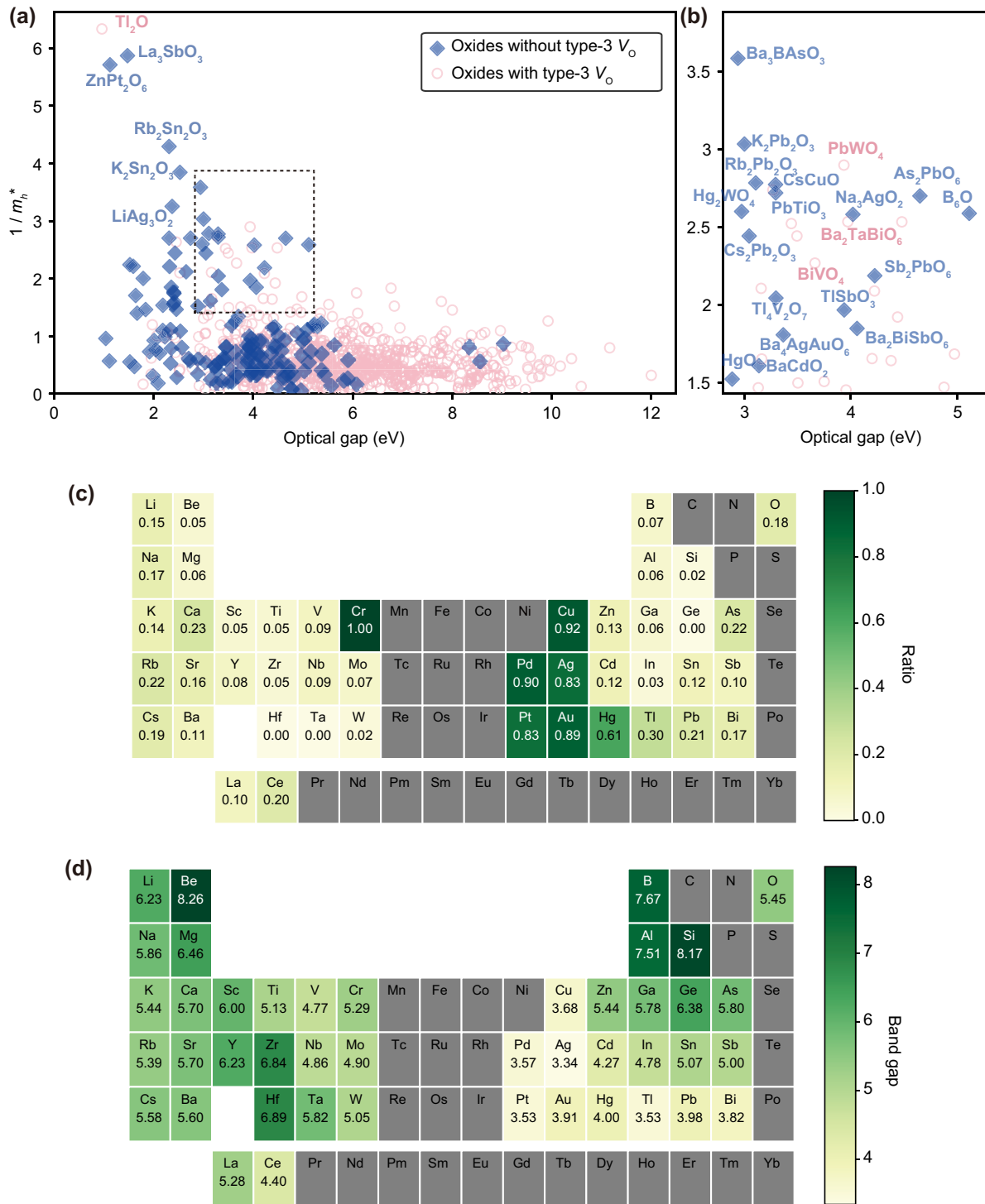


FIG. 2. (a) Plot of the reciprocal of the minimum effective hole mass ( $m_h^*$ ) against the optical gap. Oxides with and without type-3 oxygen vacancies are distinguished by symbols and colors (see the text for details). (b) Magnification of the dashed rectangle in (a). (c) Proportion of oxides with only type-1 and/or -2 oxygen vacancies, and (d) averaged optical gap of the oxides for each element. Only results with five or more oxides containing each element are shown. Overall averages are shown for the O element.

becomes zero corresponds to a pinning level, from which  $\Delta\epsilon_F$  cannot be lowered, even with acceptor doping

In this study, we assume that the chemical potentials are controllable within the stable region in the chemical-

potential diagram, and we consider O-rich conditions where oxygen vacancies are most suppressed.

The oxides without type-3 oxygen vacancies are good candidates for *p*-type TCOs because the oxygen vacancies are not dominant hole killers. We therefore classify the

oxides according to whether they have type-3 oxygen vacancies.

The inverse of  $m_h^*$  as a function of the optical gap is shown in Fig. 2(a). Note that the mobility is inversely proportional to the effective mass [Eq. (1)]. In some studies, the average hole effective mass is used as a screening parameter, assuming the application of polycrystals. We use the minimum effective mass because the crystal orientation can be controlled by adjusting the substrate and/or growth conditions. It is worth noting that, as the optical gap increases,  $m_h^*$  tends to increase in Fig. 2(a). This is partly because hybridization near the valence and conduction bands generally decreases as the band gap increases, resulting in a less-dispersive band structure.

From Fig. 2(c), which shows the proportion of oxides with only type-1 and/or -2 oxygen vacancies for each element, a clear elemental bias can be seen. The oxides mainly belong to the following three groups:

(1) Group A, the oxides of the elements with fully or partially filled  $d$  electrons in the valence bands. Examples are Pd, Pt, Cu, Ag, and Au oxides. The  $p$ -type dopability is attributed to their higher-energy levels than the O  $2p$  bands, as proposed by Kawazoe *et al.* [7].

(2) Group B, the oxides containing elements with lone-pair electrons. Examples include Tl, Sn, Pb, As, Sb, and Bi oxides. Their  $p$ -type doping is more plausible because their lone-pair bands also tend to have higher-energy levels than the O  $2p$  bands. This idea is also a common strategy to achieve  $p$ -type doping in oxides, e.g., SnO [58].

(3) Group C, the oxides of elements with empty  $d$  orbitals near the band edges. Examples include Cr, Zr, and Re oxides. The  $d^0$  orbitals form covalent bonds with O  $2p$  orbitals, resulting in greater band dispersion with higher valence-band maxima. This is less commonly considered for  $p$ -type doping so far.

The exceptions that do not belong to the three groups are  $B_6O$ ,  $Ca_3(BO_3)_2$ ,  $CaCdO_2$ ,  $Na_2ReO_3$ ,  $Sr_3(BO_3)_2$ , and ZnO. Since ZnO and  $CaCdO_2$  have filled  $d$  orbitals, even though their energy levels are much lower than O  $2p$ , they are placed in group A in the broad sense. Therefore, the remaining exceptions are  $B_6O$ ,  $Ca_3(BO_3)_2$ , and  $Sr_3(BO_3)_2$ , which result in the last group:

(1) Group D, boron oxides, in which the oxygen atoms are closely bonded to the boron atoms, resulting in higher oxygen-vacancy formation energies.

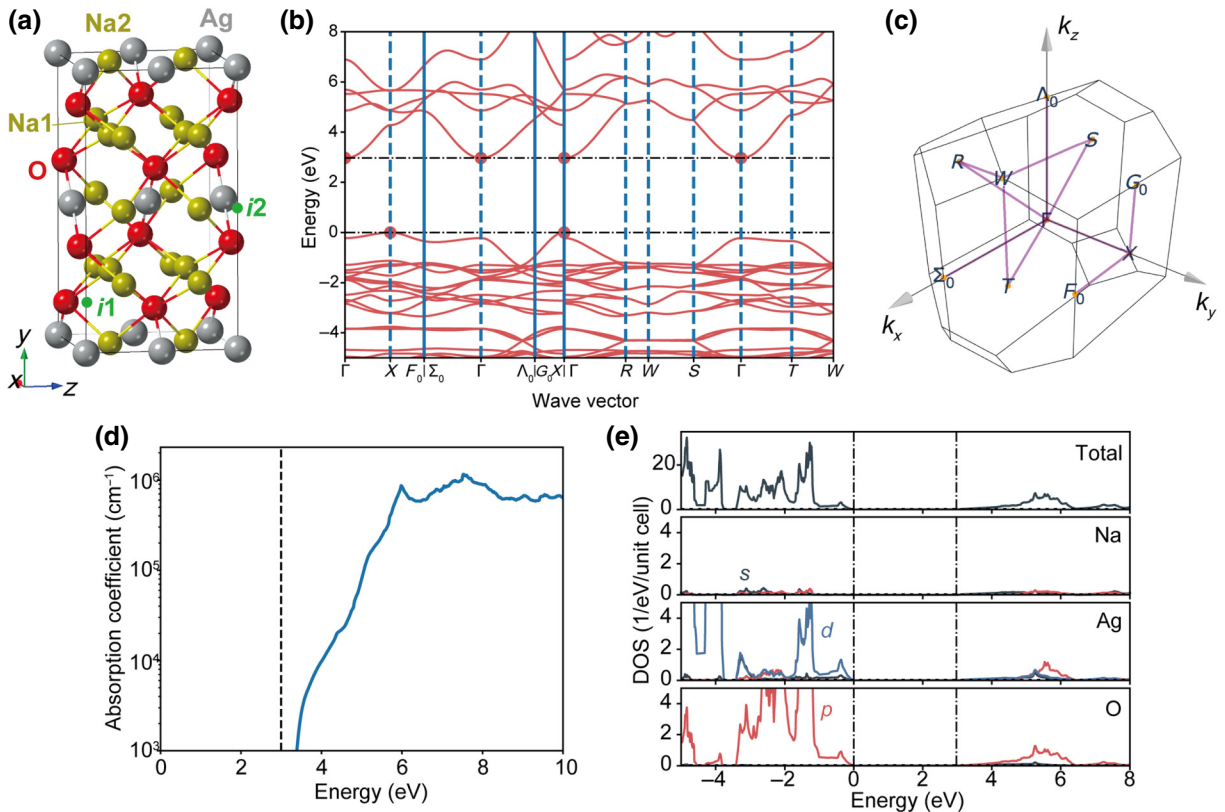


FIG. 3. (a) Conventional unit cell, (b) band structure, (c) Brillouin zone, (d) optical absorption spectrum, and (e) total and atom-projected DOS of  $Na_3AgO_2$ . In (a), the interstitial sites  $i1$  and  $i2$  are also shown as small green spheres, which are located at  $(0.3125, 0.1597, 0.0625)$  and  $(0, 0.5, 0)$  in fractional coordinates, respectively. Inequivalent Na sites are distinguished. Band path in (b) is drawn with purple lines in (c). Atom-projected DOS are obtained by summing the DOS for the same element in the primitive unit cell.

Although the optical gap should be larger than 3.1 eV for TCs [5], we use a slightly smaller criterion of 2.8 eV in anticipation of the error of the DD hybrid functionals (see Fig. S1 within the Supplemental Material [59]). An enlarged view of the dashed rectangle in Fig. 2(a) is shown in Fig. 2(b), where the oxides have an optical gap larger than 2.8 eV. Smaller  $m_h^*$  is more desirable, as long as transparency is achieved in the visible range. Only 156 out of the 845 oxides are found not to have type-3 oxygen vacancies. Such a small proportion is expected from the fact that *p*-type doping of oxides is generally difficult.

It is usually more desirable to suppress charged oxygen vacancies as much as possible to achieve *p*-type dopability. Therefore, in the Supplemental Material [59], we show the screening results with a tighter condition of  $E_f[V_O] = 1.0$  eV. We find that the number of oxides with only type-1 and/or -2 oxygen vacancies decreases from 156 to 122. However, among the superior candidates in the enlarged view in Fig. 2(b), only oxides containing toxic elements, such as  $\text{Hg}_2\text{WO}_4$  and  $\text{As}_2\text{PbO}_6$ , are excluded.

Previously identified oxides are also present in Fig. 2(b), but some of them are screened out by the presence of type-3 oxygen vacancies. An example is  $\text{Ba}_2\text{TaBiO}_6$ . Bhatia *et al.* [12] reported that  $\text{Ba}_2\text{TaBiO}_6$  had high visible-light transmittance and hole mobility larger than  $30 \text{ cm}^2/(\text{V s})$ . However, the hole concentration reaches only  $10^{14} \text{ cm}^{-3}$ , even with a large amount of K doping. The authors attribute this to the strong compensation by donors, such as oxygen vacancies. This illustrates the usefulness of  $E_f[V_O]$  as a screening parameter.

As shown in Fig. 2(d), the oxides with Be, B, Mg, Al, and Si tend to have large optical gaps, but they tend to have type-3 oxygen vacancies, as shown in Fig. 2(c). Such conflicting trends indicate the difficulty in finding *p*-type TCOs.

The fundamental band gaps, optical gaps, and  $m_h^*$  values of the seven oxides with small  $m_h^*$  values and optical gaps larger than 2.8 eV are listed in Table I, along with those of  $\text{CuAlO}_2$  calculated in this study.  $\text{Na}_3\text{AgO}_2$ ,  $\text{Rb}_2\text{Pb}_2\text{O}_3$ ,  $\text{Cs}_2\text{Pb}_2\text{O}_3$ , and  $\text{Ba}_3\text{BaSO}_3$  are identified as potential *p*-type TCOs.  $\text{K}_2\text{Pb}_2\text{O}_3$  and  $\text{B}_6\text{O}$  were proposed by Hautier

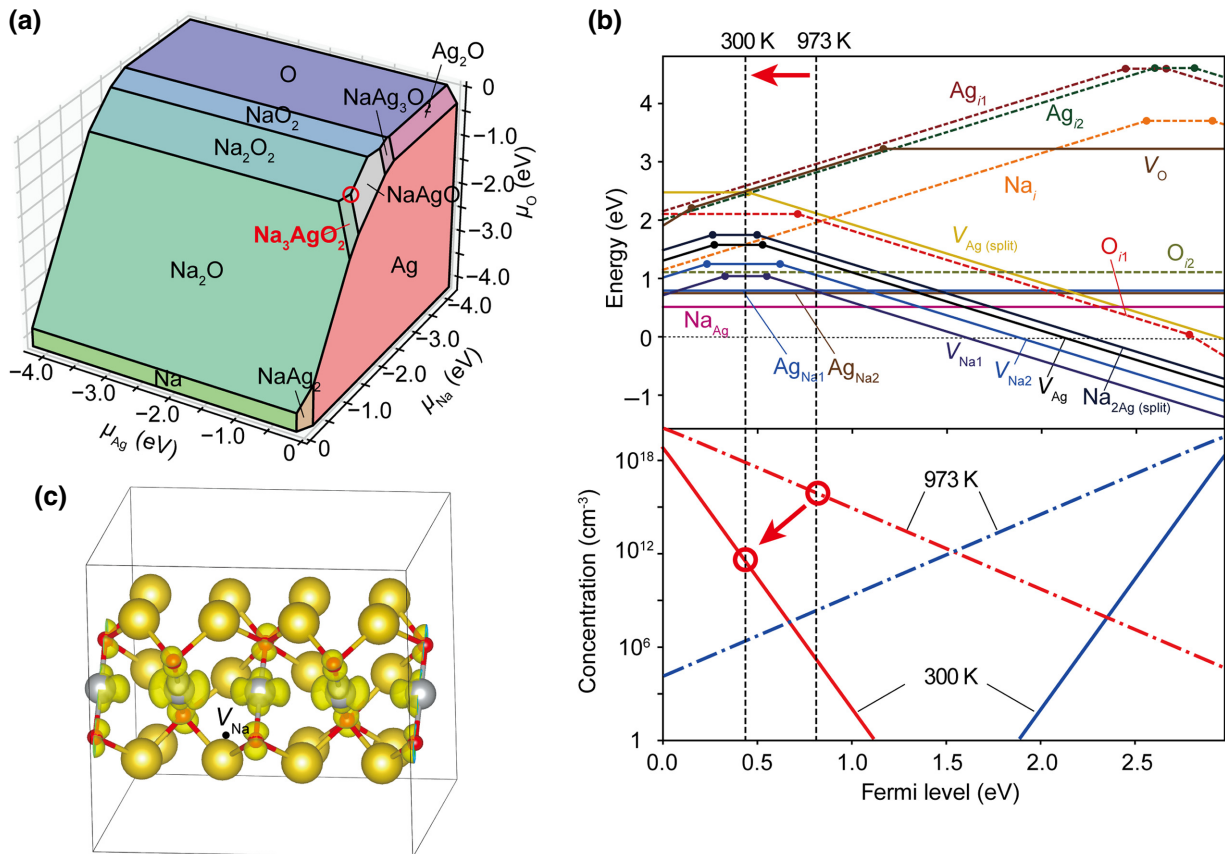


FIG. 4. (a) Na-Ag-O chemical-potential diagram. (b) Defect-formation energies in  $\text{Na}_3\text{AgO}_2$  under the O-rich condition indicated by the red circle in (a). See the text for definitions of defect notations. Carrier concentrations at  $T = 973$  and 300 K are shown at the bottom. Vertical lines indicate the Fermi level (see text for details). Interstitial sites are shown in Fig. 3(a). (c) Squared wave function of the unoccupied deep state in the calculation of  $V_{\text{Na}1}^0$  drawn using VESTA [62]. Isosurface corresponds to 10% of the maximum value.

*et al.* [8]. Yim *et al.* identified CsCuO, but they did not calculate the defect properties. The point defects in B<sub>6</sub>O are thoroughly studied, but it may be difficult to control the hole concentration in B<sub>6</sub>O because the acceptor-type defects have large formation energies [60].

The crystal and electronic structures of Rb<sub>2</sub>Pb<sub>2</sub>O<sub>3</sub> and Cs<sub>2</sub>Pb<sub>2</sub>O<sub>3</sub> are almost identical to those of K<sub>2</sub>Pb<sub>2</sub>O<sub>3</sub> (see Table I and Fig. S6 within the Supplemental Material [59]). Because Ba<sub>3</sub>BasO<sub>3</sub> contains highly toxic As, its commercial use would be extremely difficult. Therefore, details of Na<sub>3</sub>AgO<sub>2</sub>, CsCuO, and K<sub>2</sub>Pb<sub>2</sub>O<sub>3</sub>, including the defect-formation energies calculated using the DD hybrid functionals, are discussed in the following sections.

### B. Na<sub>3</sub>AgO<sub>2</sub>

The crystal structure of Na<sub>3</sub>AgO<sub>2</sub> [61] is shown in Fig. 3(a) [60]. The Na<sup>+</sup> ions are tetrahedrally coordinated to O<sup>2-</sup> ions, while the Ag<sup>+</sup> ions are surrounded by two O<sup>2-</sup> ions. Such dumbbell-type coordination is commonly observed in Cu and Ag oxides with closed 3*d* and 4*d* shells, respectively, as represented by Cu<sub>2</sub>O and Ag<sub>2</sub>O.

The calculated band structure, Brillouin zone, and optical absorption spectrum of Na<sub>3</sub>AgO<sub>2</sub> are shown in Figs. 3(b)–(d). Na<sub>3</sub>AgO<sub>2</sub> has an indirect-type band structure, where the VBM and the conduction-band minimum

are located at the *X* and  $\Gamma$  points, respectively. The difference between the fundamental band gap and the optical gap is 1.0 eV [Fig. 3(d)]. As predicted in this study, single-crystal Na<sub>3</sub>AgO<sub>2</sub> is reported to exhibit transparency in experiments [61].

The small  $m_h^*$  of 0.39  $m_0$ , where  $m_0$  is the free-electron rest mass, manifests only in the  $X \rightarrow G_0$  direction, which is parallel to  $k_z$ . Because the valence band is composed of hybridized Ag 4*d* and O 2*p* orbitals, as shown in the DOS [Fig. 3(e)], the small  $m_h^*$  is attributed to the 1D Ag-O bonding in the *z* direction [see Fig. 3(a)].

Because hybridization between the Ag 4*d* and O 2*p* orbitals pushes up the VBM, *p*-type dopability is expected [7]. The Na-Ag-O chemical-potential diagram and defect-formation energies in Na<sub>3</sub>AgO<sub>2</sub> under the oxygen-rich condition are shown in Fig. 4. Although the oxygen vacancies are doubly positively charged at the VBM,  $E_f[V_O]$  is sufficiently large not to compensate for the holes. The cation antisites (Na<sub>Ag</sub> and Ag<sub>Na</sub>) are in the neutral charge state, while the cation vacancies ( $V_{Na}$  and  $V_{Ag}$ ) act as acceptors up to  $\Delta\varepsilon_F \approx 0.5$  eV. The split-type Ag vacancy ( $V_{Ag(\text{split})}$ ) and the split-type Na-on-Ag antisite (Na<sub>2Ag(\text{split})}</sub>) act as acceptors, but they have larger formation energies than those of the vacancies and antisites. All the interstitials have larger formation energies. Two different sites,

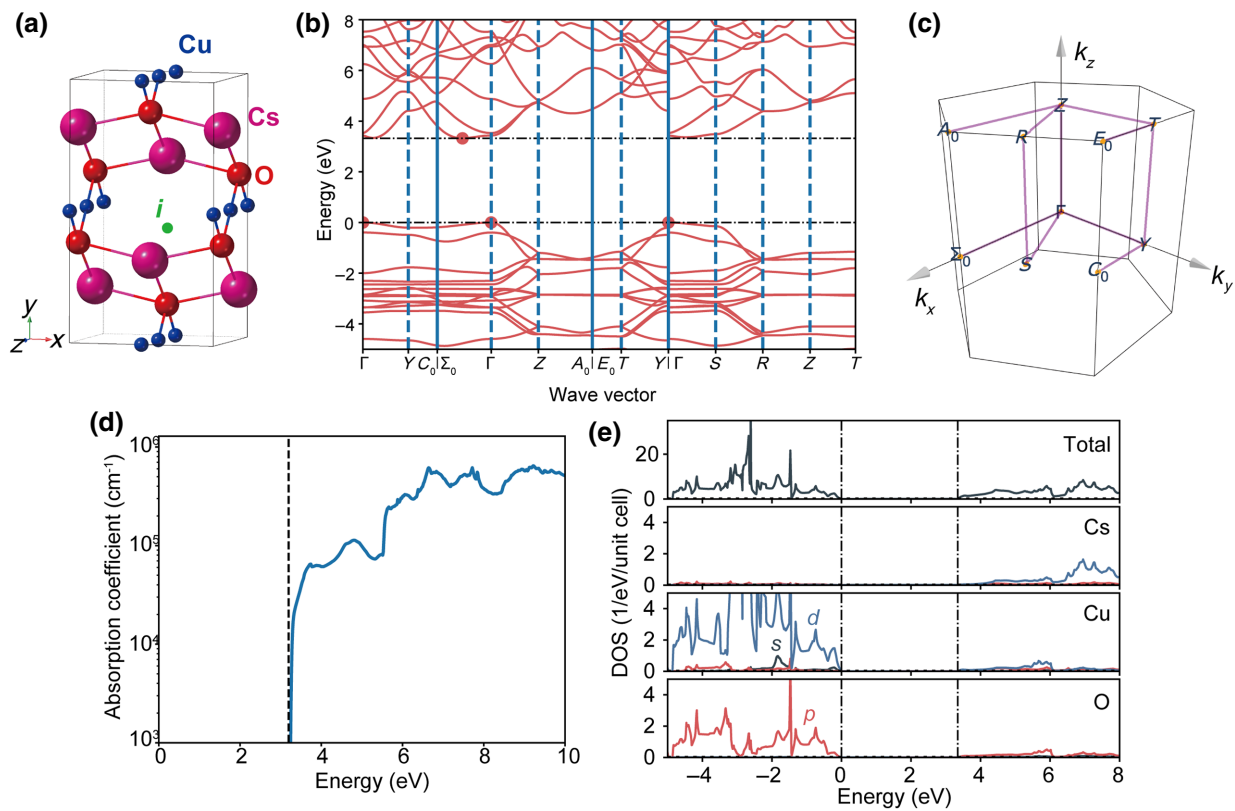


FIG. 5. (a) Conventional unit cell, (b) band structure, (c) Brillouin zone, (d) optical absorption spectrum, and (e) total and atom-projected DOS of CsCuO. Interstitial site (*i*) in (a) is located at (0.5, 0.4167, 0.25) in fractional coordinates.

shown in Fig. 4(a), are calculated for each interstitial. While Ag and O interstitials are relaxed to different defect structures [ $\text{Ag}_{ix}$  and  $\text{O}_{ix}$ , ( $x = 1, 2$ )], respectively, Na interstitials ( $\text{Na}_i$ ) converge to the same structure. In particular,  $\text{O}_{i1}$  and  $\text{O}_{i2}$  have very different formation energies and transition levels.

Next, we show the equilibrium Fermi level at the sample-growth temperature ( $T = 973$  K) [61] [Fig. 4(b)]. The calculated hole concentration ( $p$ ) is  $1 \times 10^{16} \text{ cm}^{-3}$ , where the concentrations ( $c$ ) of dominant defects are  $c(V_{\text{Na}}^{-1}) = 1 \times 10^{16} \text{ cm}^{-3}$ ,  $c(\text{Na}_{\text{Ag}}^0) = 8 \times 10^{20} \text{ cm}^{-3}$ , and  $c(\text{Ag}_{\text{Na}}^0) = 2 \times 10^{17} \text{ cm}^{-3}$ . However, when the temperature is lowered to 300 K,  $p$  is reduced to  $3 \times 10^{11} \text{ cm}^{-3}$ , mainly due to the thermodynamic transition of  $V_{\text{Na}1}$  at  $\Delta\epsilon_F = 0.55$  eV. As shown in the bottom of Fig. 4(b), when the temperature is decreased, the Fermi level is decreased, as long as  $p$  is constant. However, when it crosses a transition level of dominant defects, most of the holes are trapped, and the Fermi level is pinned near the transition

level. Indeed, the concentration of  $V_{\text{Na}1}$  is redistributed to  $c(V_{\text{Na}}^{-1}) = 5 \times 10^{13} \text{ cm}^{-3}$  and  $c(V_{\text{Na}1}^0) = 1 \times 10^{16} \text{ cm}^{-3}$  at  $T = 300$  K. The close transition levels also appear in  $V_{\text{Na}2}$ ,  $V_{\text{Ag}}$ , and  $\text{Na}_{2\text{Ag}(\text{split})}$ .

To study the transition levels, we plot the squared wave function of the unoccupied deep state in the calculation of  $V_{\text{Na}1}^0$  in Fig. 4(c). The hole is distributed along a Ag-Ag chain as a 1D polaronic state. Such a 1D state is also found for  $V_{\text{Na}2}^0$ ,  $V_{\text{Ag}}^0$ , and  $\text{Na}_{2\text{Ag}(\text{split})}^0$ . Since the effective mass along this direction is very small (see Table I), high hole conductivity can be achieved only in this direction, if a sufficient number of polarons are introduced.

To introduce more hole polarons, acceptor-type doping is more desirable. Traditionally, acceptor dopants are ions with a lower valence than the constituent atoms. For oxides, cation doping is more desirable because it can be achieved simply by sintering the oxides with the dopants. However, in the case of *p*-type doping of monovalent cation oxides, there are no oxides consisting of zero-valence elements. To overcome this, Matsuzaki

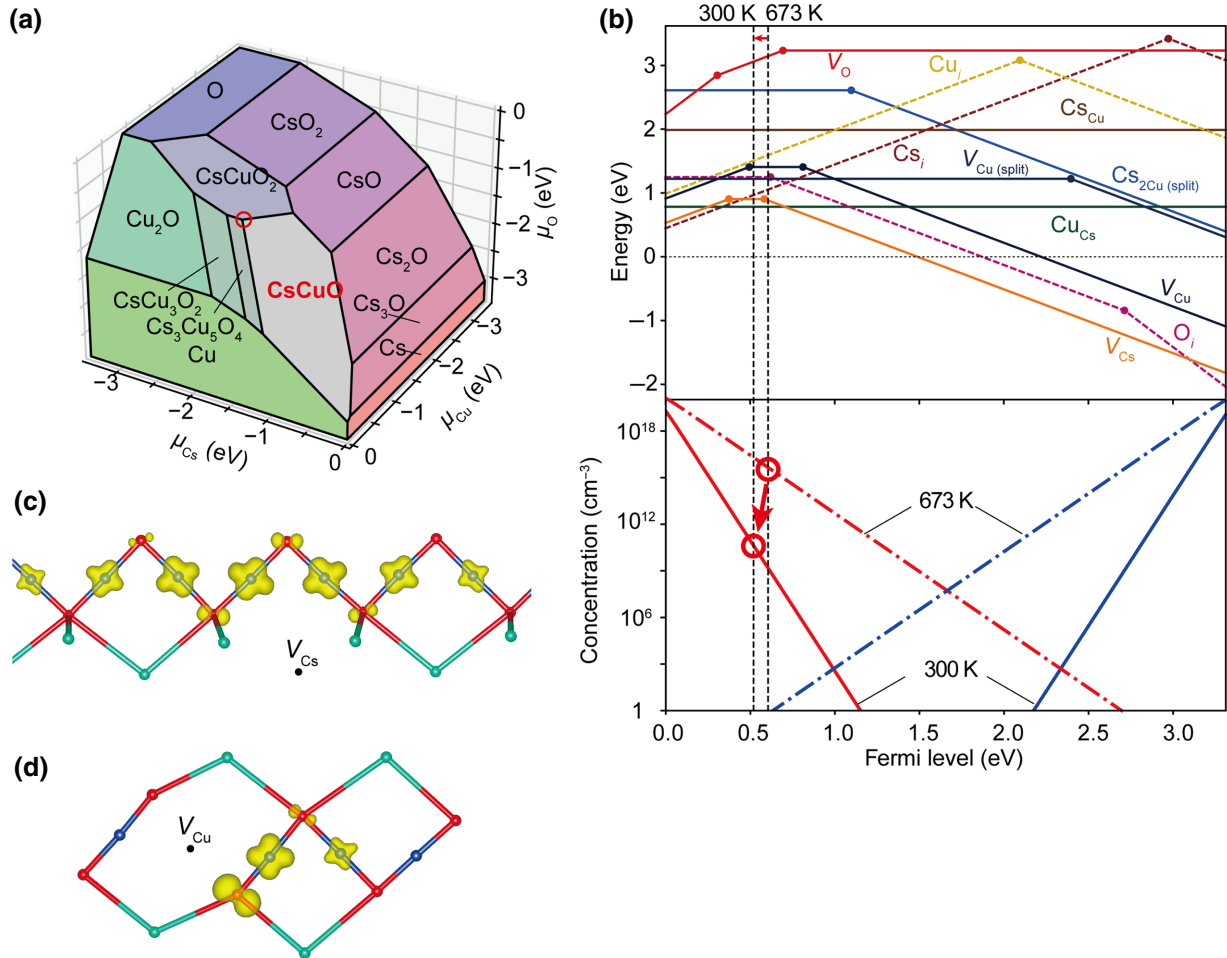


FIG. 6. (a) Cs-Cu-O chemical-potential diagram. (b) Defect-formation energies in CsCuO under the O-rich condition indicated by the red circle in (a). Interstitial site is shown in Fig. 5(a). Squared wave function of unoccupied deep state in the calculation of (c)  $V_{\text{Cs}}^0$  and (d)  $V_{\text{Cu}}^0$ . Isosurfaces correspond to 10% of their respective maxima.

*et al.* [63] proposed to dope isovalent ions with larger ionic radii than the constituent cations. For example, the hole-carrier concentration in  $\text{Cu}_2\text{O}$  is increased by doping Na, which has the same valence as copper but a larger size. Thus, as the size mismatch with  $\text{Cu}^+$  in the host lattice is increased, these isovalent impurities are preferentially located in interstitial positions to form stable acceptor-like impurity-defect complexes. Because Ag is located in the same column as Cu in the periodic table, the same hole-doping strategy can be expected for Ag compounds.

To verify that this doping strategy works well in  $\text{Na}_3\text{AgO}_2$ , we calculate the K dopants. As shown in Fig. S3 within the Supplemental Material [59], the K dopants located at the interstitial sites with two Ag vacancies ( $\text{K}_{2\text{Ag}(\text{split})}$ ) have lower formation energies than  $\text{Na}_{2\text{Ag}(\text{split})}$ , but higher than  $V_{\text{Na}1}$ . Therefore, nonthermal-equilibrium doping is more desirable when K is doped.

### C. CsCuO

The unit cell and electronic structure of CsCuO [61] are shown in Fig. 5. Like  $\text{Ag}^+$  in  $\text{Na}_3\text{AgO}_2$ , the  $\text{Cu}^+$  ions are coordinated to two  $\text{O}^{2-}$  ions. The band structure indicates an indirect gap with the VBM located at the  $\Gamma$  point, but the difference between the direct and indirect gaps is

negligible.  $m_h^*$  is very small ( $0.36m_0$ ) along the  $\Gamma \rightarrow Z$  ( $k_z$ ) direction. The single crystal of CsCuO is also known to exhibit transparency, which is consistent with this study [64].

In the DOS [Fig. 5(e)], the valence bands are composed of hybridized Cu  $3d$  and O  $2p$  orbitals, and thus, the small  $m_h^*$  is attributed to the Cu-O channel along the  $z$  direction, as shown in Fig. 5(a), which is similar to  $\text{Na}_3\text{AgO}_2$ .

$m_h^*$  is closely related to the crystal structure. When Cs is replaced by Na, K, or Rb, the structure changes to the  $I4/mmm$  phase (see Fig. S4 within the Supplemental Material [59]). In this structure,  $m_h^*$  increases significantly from  $0.36m_0$  to  $1.89\text{--}3.21m_0$  because the Cu-O bonding pathway is interrupted by the alkali-metal ions. Therefore, the continuous bonding that constitutes the VBM in real space is the key to low  $m_h^*$ .

The Cs-Cu-O chemical-potential diagram and the defect-formation energies in CsCuO under the O-rich condition are shown in Fig. 6. The large area of CsCuO in the chemical-potential diagram indicates its high stability with respect to the competing phases. The defect-formation energies show a similar tendency to those in  $\text{Na}_3\text{AgO}_2$ . The formation energy of the oxygen vacancy is large even at  $\Delta\varepsilon_F = 0$ , while the cation vacancies ( $V_{\text{Cs}}$  and  $V_{\text{Cu}}$ ) act as acceptors with relatively small formation energies

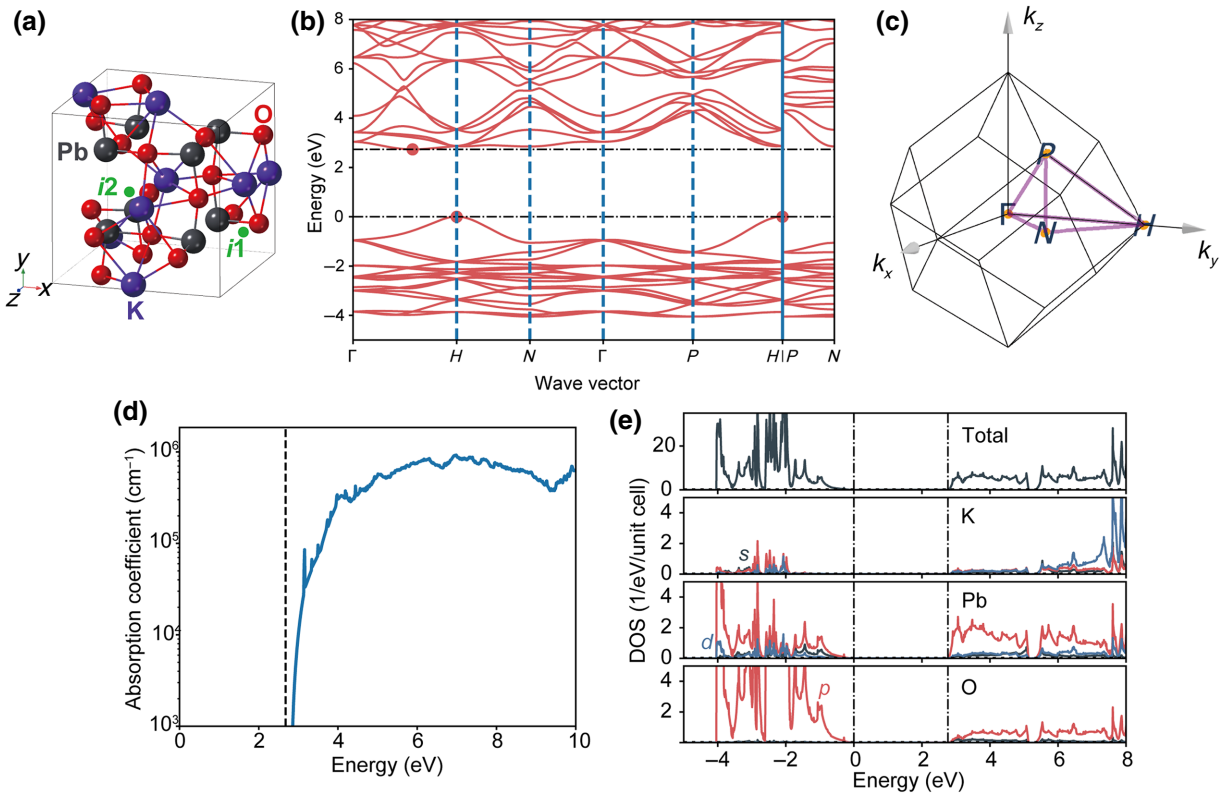


FIG. 7. (a) Conventional unit cell, (b) band structure, (c) Brillouin zone, (d) optical absorption spectrum, and (e) total and atom-projected DOS of  $\text{K}_2\text{Pb}_2\text{O}_3$ . Interstitial sites  $i1$  and  $i2$  in (a) are located at  $(0.9948, 0.2691, 0.5556)$  and  $(0.3009, 0.4398, 0.5185)$  in fractional coordinates, respectively.

[Fig. 6(b)]. However, in contrast to  $\text{Na}_3\text{AgO}_2$ , the anti-site defects ( $\text{Cs}_{\text{Cu}}$  and  $\text{Cu}_{\text{Cs}}$ ) have large formation energies due to the large ionic size mismatch between Cs and Cu (1.67 vs 0.46 Å in the four-coordination number) [65]. The split-type interstitial ( $\text{Cs}_{2\text{Cu}(\text{split})}$ ), where Cs is located at the center of two copper vacancies ( $V_{\text{Cu}}$ ), has a larger energy than the cesium vacancy ( $V_{\text{Cs}}$ ) and  $V_{\text{Cu}}$ . The Cu and O interstitials ( $\text{Cu}_i$  and  $\text{O}_i$ ) have relatively large formation energies. On the contrary, despite the large ionic size of Cs, the Cs interstitial ( $\text{Cs}_i$ ) is the dominant donor at  $\Delta\varepsilon_F$  located near the VBM, mainly due to the large voids in the Cs layers [see Fig. 5(a)].

The equilibrium Fermi levels at  $T = 673$  and 300 K are also shown in Fig. 6(b). Although the equilibrium hole concentration at 673 K is  $5 \times 10^{15} \text{ cm}^{-3}$ , which is mainly caused by  $V_{\text{Cs}}^{-1}$ , it is largely reduced to  $4 \times 10^{10} \text{ cm}^{-3}$  at 300 K as in  $\text{Na}_3\text{AgO}_2$  mainly because  $V_{\text{Cs}}$  trap holes as shown in Fig. 6(b). To understand the origin of the deep state, we plot the squared wave function of the unoccupied deep state in the calculation of  $V_{\text{Cs}}^0$  and  $V_{\text{Cu}}^0$  in Figs. 6(c) and 6(d). It is found that a 1D polaronic state exists near  $V_{\text{Cs}}^0$ , while a small polaron is distributed at the Cu and O sites near the Cu vacancy. The difference would be mainly because the 1D Cu-Cu structure is broken by  $V_{\text{Cu}}^0$ . If the small polaronic states are dominant, it would be difficult to introduce carrier holes, even with *p*-type doping.

## D. $\text{K}_2\text{Pb}_2\text{O}_3$

The crystal structure, band structure, optical absorption spectrum, and DOS of  $\text{K}_2\text{Pb}_2\text{O}_3$  are shown in Fig. 7. The  $6s^2$  lone-pair electrons of the  $\text{Pb}^{2+}$  ions in  $\text{K}_2\text{Pb}_2\text{O}_3$  point to free space (see Fig. S5 within the Supplemental Material [59] for the electron-localization function) [66].  $\text{K}_2\text{Pb}_2\text{O}_3$  also has an indirect-type band structure with the VBM at the *H* point. The valence band is mainly composed of hybridized Pb *6s* and O *2p* orbitals. Unlike  $\text{Na}_3\text{AgO}_2$  and  $\text{CsCuO}$ ,  $\text{K}_2\text{Pb}_2\text{O}_3$  has a small  $m_h^*$  in all directions because of the three-dimensional Pb-O network.

Experimentally, single-crystal  $\text{K}_2\text{Pb}_2\text{O}_3$  with  $\phi = 5$  mm is reported to be clearly transparent with an orange color [67]. It is difficult to explain the origin of the color, but if it is caused by the defects, such coloration can be reduced by changing the growth conditions, so experimental verification is highly desirable.

The K-Pb-O chemical-potential diagram and defect-formation energies in  $\text{K}_2\text{Pb}_2\text{O}_3$  under the O-rich condition are shown in Fig. 8. The vacancy properties are similar to those of  $\text{Na}_3\text{AgO}_2$  and  $\text{CsCuO}$ . The oxygen vacancies have large formation energies, while the cation vacancies ( $V_{\text{Pb}}$  and  $V_{\text{K}}$ ) act as acceptors with relatively small formation energies. In contrast, because K and Pb have different oxidation states, K-on-Pb ( $\text{K}_{\text{Pb}}$ ) and Pb-on-K ( $\text{Pb}_{\text{K}}$ ) act as a single acceptor and a single donor, respectively, in the *p*-type region. We calculate two different sites for each

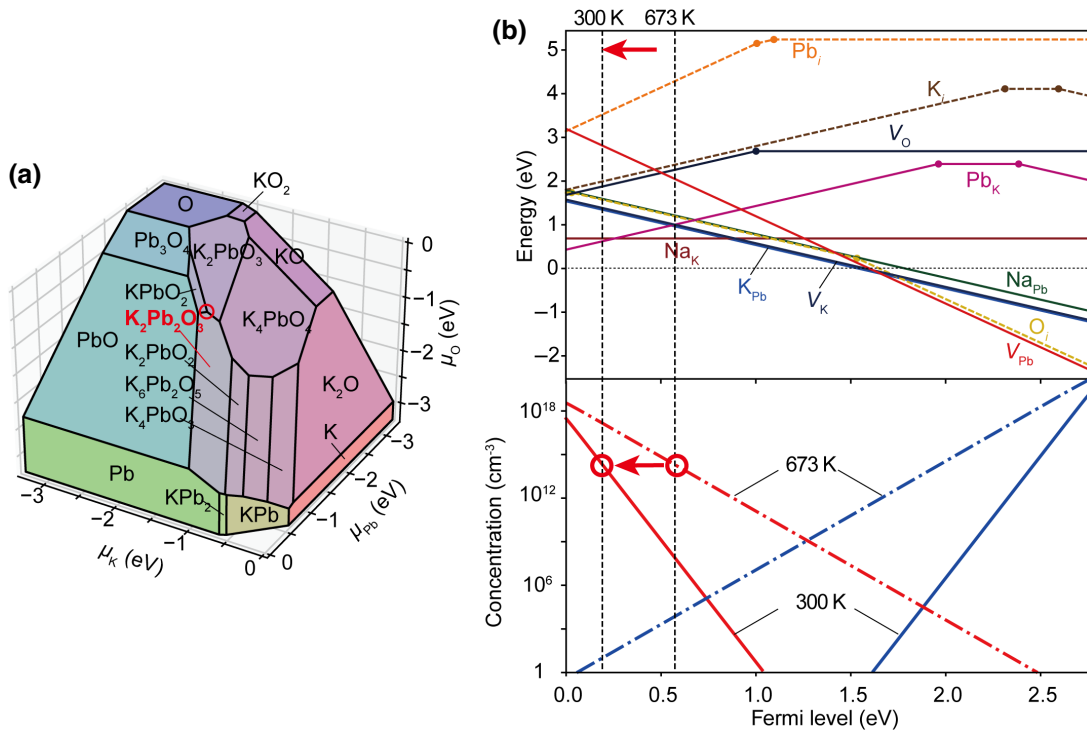


FIG. 8. (a) K-Pb-O chemical-potential diagram. (b) Defect-formation energies in  $\text{K}_2\text{Pb}_2\text{O}_3$  under the O-rich condition designated in (a). Na chemical potential is determined from the  $\text{Na}_2\text{PbO}_3$  total energy. Formation energies of the Na dopant are also shown. Interstitial sites are shown in Fig. 7(a).

interstitial, as shown in Fig. 7(a) but find that they are relaxed to the same defect structure. The cation interstitials ( $K_i$  and  $Pb_i$ ) act as deep donors with relatively large formation energies, while the oxygen interstitials ( $O_i$ ) act as shallow acceptors with formation energies comparable to those of the other dominant acceptors.

Hautier *et al.* [8] also identified  $K_2Pb_2O_3$  as a promising  $p$ -type TCO, and they calculated the vacancies ( $V_O$ ,  $V_{Pb}$ , and  $V_K$ ) using the PBE functional with band-edge corrections in the  $G_0W_0$  approximation. Our calculated vacancy formation energies are similar to their results, but the  $-1/-2$  and  $-2/-4$  transition levels of  $V_{Pb}$  in Ref. [8] do not appear in our calculations.

To verify hole doping by impurities, we calculate the defect-formation energies of Na dopants because the ionic radius of  $Na^+$  (1.16 Å in the six coordinate [65]) is closer to that of  $Pb^{2+}$  (1.33 Å) than to that of  $K^+$  (1.52 Å). As shown in Fig. 8(b), in the  $p$ -type regime, although the Na impurities are mainly located at the K sites in the neutral charge states, they also exist in the negatively charged state at the Pb site ( $Na_{Pb}$ ). Because  $Na_{Pb}$  has a larger formation energy, nonthermal-equilibrium doping is desired for further hole doping.

Our screening also identifies  $Rb_2Pb_2O_3$  and  $Cs_2Pb_2O_3$  as potential  $p$ -type TCOs, which are isostructural to  $K_2Pb_2O_3$ . In fact, their electronic structures and band gaps are almost identical (Table I and Fig. S6 in the Supplemental Material [59]). The disadvantage of  $A_2Pb_2O_3$  ( $A = K, Rb, Cs$ ) is that it contains toxic Pb ions. Unfortunately, replacing Pb with Sn reduces the band gaps to values unsuitable for TCOs [8].

Although  $CsCuO$  and  $K_2Pb_2O_3$  were previously proposed as potential  $p$ -type TCOs [8], they have not attracted much attention [9]. This is partly because the band gaps of  $CsCuO$  and  $K_2Pb_2O_3$  calculated by the HSE functional and the  $GW_0$  approximation, respectively, are 2.45 and 2.6 eV, which are smaller than the desirable gap of 3.1 eV. However, it should be kept in mind that accurate prediction of the band gap is generally not an easy task [11], even using high-level approximations. For example, the calculated band gap of  $Ba_2TaBiO_6$  using the  $G_0W_0$  approximation is 3.8 eV, while the experimental gap is reported to range between 3.2 and 5.0 eV [12,68]. Therefore, experimental verification is essential to determine whether the screened oxides truly exhibit high performance as  $p$ -type TCOs.

#### IV. DISCUSSION AND CONCLUSIONS

We screen potential  $p$ -type TCOs using the optical absorption spectra and effective masses calculated with accurate DD hybrid functionals and the formation energies of oxygen vacancies, which are the main hole killers in oxides. Consequently, we identify six potential

$p$ -type TCOs.  $Na_3AgO_2$  is identified as a potential  $p$ -type TCO, while the previously proposed  $p$ -type TCOs  $CsCuO$ ,  $K_2Pb_2O_3$ , and  $B_6O$  are also identified.  $Rb_2Pb_2O_3$  and  $Cs_2Pb_2O_3$  are identified as  $p$ -type TCOs, but they are found to have almost identical properties to those of  $K_2Pb_2O_3$ . For  $Na_3AgO_2$ ,  $CsCuO$ , and  $K_2Pb_2O_3$ , we calculate the vacancies, antisites, and interstitials using DD hybrid functionals. They are predicted to be  $p$ -type semiconductors, even without external doping.

Many of the previously proposed  $p$ -type TCOs are rediscovered in this study, indicating that previous screening studies work satisfactorily. However, we would like to emphasize that the importance of our screening is that it allows us to remove a large fraction of inappropriate oxides based on  $E_f[V_O]$ . Indeed, only 156 out of the 845 oxides are found to have benign oxygen vacancies for  $p$ -type doping. Eliminating such false-positive candidates should increase the success rate of finding  $p$ -type TCOs in labor-intensive experiments.

We would like to emphasize that, although the  $p$ -type TCOs are screened based on the formation energies of oxygen vacancies, it is essential to calculate all possible point defects for the screened candidates for the following reasons. First, other hole killers may be present. In particular, cation antisites are very likely in oxides composed of two or more cations. Second, to achieve  $p$ -type doping, we need to know the formation energies of acceptor-type defects and acceptor dopants. Indeed, we find that  $Na_3AgO_2$  and  $CsCuO$  exhibit 1D polaronic behavior, which would prevent high conductivity in three-dimensional directions. Furthermore, it is preferable to perform these calculations at the hybrid functional level to increase the predictive power.

We also note that some research shows that hydrogen passivation with hole-killer defects can avoid the incorporation of oxygen vacancies [69]. This technique, in fact, is successfully used to obtain  $p$ -type gallium nitrides [70]. Therefore, the rejected oxides in this study should not be completely dismissed for future consideration.

In the future, the accuracy of band gaps will be improved and the optical absorption spectra and point-defect formation energies will be published in publicly available computational databases, such as the Materials Project database [21]. This study serves as a good example of the use of these datasets. In addition, our calculated optical absorption spectra, band structures, and effective masses, which are available in the GitHub repository [71], will also be useful for screening other classes of materials, such as solar-cell absorbates and light-emitting diodes.

#### ACKNOWLEDGMENTS

We greatly appreciate S. Iimura and K. Matsuzaki for fruitful discussions. This study is financially supported by PRESTO (Grant No. JPMJPR16N4) from the

Japan Science and Technology Agency; KAKENHI (Grant No. 22H01755); and the E-IMR project at IMR, Tohoku University.

- 
- [1] A. Stadler, Transparent conducting oxides—an up-to-date overview, *Materials* **5**, 661 (2012).
- [2] A. Facchetti and T. J. Marks, *Transparent Electronics: From Synthesis to Applications* (John Wiley & Sons, Ltd, West Sussex, 2010).
- [3] T. Minami, Present status of transparent conducting oxide thin-film development for indium-tin-oxide (ITO) substitutes, *Thin Solid Films* **516**, 5822 (2008).
- [4] K. Nomura, H. Ohta, A. Takagi, T. Kamiya, M. Hirano, and H. Hosono, Room-temperature fabrication of transparent flexible thin-film transistors using amorphous oxide semiconductors, *Nature* **432**, 488 (2004).
- [5] K. H. L. Zhang, K. Xi, M. G. Blamire, and R. G. Egdell, *p*-Type transparent conducting oxides, *J. Phys.: Condens. Matter* **28**, 383002 (2016).
- [6] X. Cai and S.-H. Wei, Perspective on the band structure engineering and doping control of transparent conducting materials, *Appl. Phys. Lett.* **119**, 070502 (2021).
- [7] H. Kawazoe, M. Yasukawa, H. Hyodo, M. Kurita, H. Yanagi, and H. Hosono, *p*-Type electrical conduction in transparent thin films of CuAlO<sub>2</sub>, *Nature* **389**, 939 (1997).
- [8] G. Hautier, A. Miglio, G. Ceder, G.-M. Rignanese, and X. Gonze, Identification and design principles of low hole effective mass *p*-type transparent conducting oxides, *Nat. Commun.* **4**, 2292 (2013).
- [9] K. Yim, Y. Youn, M. Lee, D. Yoo, J. Lee, S. H. Cho, and S. Han, Computational discovery of *p*-type transparent oxide semiconductors using hydrogen descriptor, *Npj Comput. Mater.* **4**, 17 (2018).
- [10] J. B. Varley, A. Miglio, V.-A. Ha, M. J. van Setten, G.-M. Rignanese, and G. Hautier, High-throughput design of non-oxide *p*-type transparent conducting materials: Data mining, search strategy, and identification of boron phosphide, *Chem. Mater.* **29**, 2568 (2017).
- [11] R. Woods-Robinson, D. Broberg, A. Faghaninia, A. Jain, S. S. Dwaraknath, and K. A. Persson, Assessing high-throughput descriptors for prediction of transparent conductors, *Chem. Mater.* **30**, 8375 (2018).
- [12] A. Bhatia, *et al.*, High-mobility bismuth-based transparent *p*-type oxide from high-throughput material screening, *Chem. Mater.* **28**, 30 (2015).
- [13] H. Peng, *et al.*, Li-doped Cr<sub>2</sub>MnO<sub>4</sub>: A new *p*-type transparent conducting oxide by computational materials design, *Adv. Funct. Mater.* **23**, 5267 (2013).
- [14] N. Sarmadian, R. Saniz, B. Partoens, and D. Lamoen, Easily doped *p*-type, low hole effective mass, transparent oxides, *Sci. Rep.-UK* **6**, 20446 (2016).
- [15] B. A. D. Williamson, J. Buckeridge, J. Brown, S. Ansbro, R. G. Palgrave, and D. O. Scanlon, Engineering valence band dispersion for high mobility *p*-type semiconductors, *Chem. Mater.* **29**, 2402 (2017).
- [16] J. P. Perdew, K. Burke, and M. Ernzerhof, Generalized Gradient Approximation Made Simple, *Phys. Rev. Lett.* **77**, 3865 (1996).
- [17] L. Hedin, New method for calculating the one-particle Green's function with application to the electron-gas problem, *Phys. Rev.* **139**, A796 (1965).
- [18] A. Walsh, *et al.*, Nature of the Band Gap of In<sub>2</sub>O<sub>3</sub> Revealed by First-Principles Calculations and X-Ray Spectroscopy, *Phys. Rev. Lett.* **100**, 167402 (2008).
- [19] X. Cai, P. Zhang, and S.-H. Wei, Revisit of the band gaps of rutile SnO<sub>2</sub> and TiO<sub>2</sub>: A first-principles study, *J. Semicond.* **40**, 092101 (2019).
- [20] X. Nie, S.-H. Wei, and S. B. Zhang, Bipolar Doping and Band-Gap Anomalies in Delafossite Transparent Conductive Oxides, *Phys. Rev. Lett.* **88**, 066405 (2002).
- [21] A. Jain, *et al.*, Commentary: The Materials Project: A materials genome approach to accelerating materials innovation, *APL Mater.* **1**, 011002 (2013).
- [22] F. K. Shan and Y. S. Yu, Band gap energy of pure and Al-doped ZnO thin films, *J. Eur. Ceram. Soc.* **24**, 1869 (2004).
- [23] M. Balog, M. Schieber, M. Michman, and S. Patai, The chemical vapour deposition and characterization of ZrO<sub>2</sub> films from organometallic compounds, *Thin Solid Films* **47**, 109 (1977).
- [24] P. Y. Yu and M. Cardona, *Fundamentals of Semiconductors Physics and Materials Properties*, 4th ed. (Springer, Berlin, 2010).
- [25] S. Ponc, W. Li, S. Reichardt, and F. Giustino, First-principles calculations of charge carrier mobility and conductivity in bulk semiconductors and two-dimensional materials, *Rep. Prog. Phys.* **83**, 036501 (2020).
- [26] S. Zhang, S. H. Wei, and A. Zunger, Intrinsic *n*-type versus *p*-type doping asymmetry and the defect physics of ZnO, *Phys. Rev. B* **63**, 075205 (2001).
- [27] P. Ágoston and K. Albe, Intrinsic *n*-Type Behavior in Transparent Conducting Oxides: A Comparative Hybrid-Functional Study of In<sub>2</sub>O<sub>3</sub>, SnO<sub>2</sub>, and ZnO, *Phys. Rev. Lett.* **103**, 245501 (2009).
- [28] N. Tsunoda, Y. Kumagai, and F. Oba, Stabilization of small polarons in BaTiO<sub>3</sub> by local distortions, *Phys. Rev. Mater.* **3**, 114602 (2019).
- [29] M. Choi, F. Oba, Y. Kumagai, and I. Tanaka, Antiferrodistortive-like oxygen-octahedron rotation induced by the oxygen vacancy in Cubic SrTiO<sub>3</sub>, *Adv. Mater.* **25**, 86 (2013).
- [30] Y. Kumagai, N. Tsunoda, A. Takahashi, and F. Oba, Insights into oxygen vacancies from high-throughput first-principles calculations, *Phys. Rev. Mater.* **5**, 123803 (2021).
- [31] J. H. Skone, M. Govoni, and G. Galli, Self-consistent hybrid functional for condensed systems, *Phys. Rev. B* **89**, 195112 (2014).
- [32] P. E. Blöchl, Projector Augmented-Wave Method, *Phys. Rev. B* **50**, 17953 (1994).
- [33] G. Kresse and D. Joubert, From ultrasoft pseudopotentials to the projector augmented-wave method, *Phys. Rev. B* **59**, 1758 (1999).
- [34] G. Kresse and J. Furthmüller, Efficient iterative schemes for *ab initio* total-energy calculations using a plane-wave basis set, *Phys. Rev. B* **54**, 11169 (1996).
- [35] J. P. Perdew, A. Ruzsinszky, G. I. Csonka, O. A. Vydrov, G. E. Scuseria, L. A. Constantin, X. Zhou, and K. Burke, Restoring the Density-Gradient Expansion for Exchange in Solids and Surfaces, *Phys. Rev. Lett.* **100**, 136406 (2008).

- [36] S. L. Dudarev, S. Y. Savrasov, C. J. Humphreys, and A. P. Sutton, Electron-energy-loss spectra and the structural stability of nickel oxide: An LSDA + U study, *Phys. Rev. B* **57**, 1505 (1998).
- [37] Y. Hinuma, G. Pizzi, Y. Kumagai, F. Oba, and I. Tanaka, Band structure diagram paths based on crystallography, *Comput. Mater. Sci.* **128**, 140 (2017).
- [38] G. K. H. Madsen, J. Carrete, and M. J. Verstraete, BoltzTraP2, a program for interpolating band structures and calculating semi-classical transport coefficients, *Comput. Phys. Commun.* **231**, 140 (2018).
- [39] Y. Kumagai, *vis*, <https://github.com/kumagai-group/vis>
- [40] A. Jain, *et al.*, FireWorks: A dynamic workflow system designed for high-throughput applications, *Concurr. Comput.: Pract. Exp.* **27**, 5037 (2015).
- [41] S. P. Ong, W. D. Richards, A. Jain, G. Hautier, M. Kocher, S. Cholia, D. Gunter, V. L. Chevrier, K. A. Persson, and G. Ceder, Python materials genomics (Pymatgen): A robust, open-source PYTHON library for materials analysis, *Comput. Mater. Sci.* **68**, 314 (2013).
- [42] Y. Hinuma, Y. Kumagai, I. Tanaka, and F. Oba, Band alignment of semiconductors and insulators using dielectric-dependent hybrid functionals: Toward high-throughput evaluation, *Phys. Rev. B* **95**, 075302 (2017).
- [43] S. van der Walt, J. L. Schönberger, J. Nunez-Iglesias, F. Boulogne, J. D. Warner, N. Yager, E. Gouillart, T. Yu, and Scikit-image contributors, Scikit-Image: Image processing in PYTHON, *PeerJ* **2**, e453 (2014).
- [44] A. F. Wright and J. S. Nelson, Theory of the copper vacancy in cuprous oxide, *J. Appl. Phys.* **92**, 5849 (2002).
- [45] Y. Kumagai, L. A. Burton, A. Walsh, and F. Oba, Electronic Structure and Defect Physics of Tin Sulfides: SnS, Sn<sub>2</sub>S<sub>3</sub>, and SnS<sub>2</sub>, *Phys. Rev. Appl.* **6**, 014009 (2016).
- [46] Y. Kumagai and F. Oba, Electrostatics-based finite-size corrections for first-principles point defect calculations, *Phys. Rev. B* **89**, 195205 (2014).
- [47] C. Freysoldt, J. Neugebauer, and C. V. de Walle, Fully *Ab Initio* Finite-Size Corrections for Charged-Defect Supercell Calculations, *Phys. Rev. Lett.* **102**, 016402 (2009).
- [48] Y. Kumagai, K. Harada, H. Akamatsu, K. Matsuzaki, and F. Oba, Carrier-Induced Band-Gap Variation and Point Defects in Zn<sub>3</sub>N<sub>2</sub> from First Principles, *Phys. Rev. Appl.* **8**, 014015 (2017).
- [49] Y. Kumagai, M. Choi, Y. Nose, and F. Oba, First-principles study of point defects in chalcopyrite ZnSnP<sub>2</sub>, *Phys. Rev. B* **90**, 125202 (2014).
- [50] T. Gake, Y. Kumagai, and F. Oba, First-principles study of self-trapped holes and acceptor impurities in Ga<sub>2</sub>O<sub>3</sub> polymorphs, *Phys. Rev. Mater.* **3**, 044603 (2019).
- [51] N. Tsunoda, Y. Kumagai, M. Araki, and F. Oba, One-dimensionally extended oxygen vacancy states in perovskite oxides, *Phys. Rev. B* **99**, 060103 (2019).
- [52] N. Tsunoda, Y. Kumagai, A. Takahashi, and F. Oba, Electrically Benign Defect Behavior in Zinc Tin Nitride Revealed from First Principles, *Phys. Rev. Appl.* **10**, 011001 (2018).
- [53] Y. Kumagai, N. Tsunoda, and F. Oba, Point Defects and *p*-Type Doping in ScN from First Principles, *Phys. Rev. Appl.* **9**, 034019 (2018).
- [54] A. Wang, R. Kingsbury, M. McDermott, M. Horton, A. Jain, S. P. Ong, S. Dwaraknath, and K. A. Persson, A framework for quantifying uncertainty in DFT energy corrections, *Sci. Rep.-UK* **11**, 15496 (2021).
- [55] Y. Kumagai, *pydefect*, <https://github.com/kumagai-group/pydefect>
- [56] S. Lany, J. Osorio-Guillén, and A. Zunger, Origins of the doping asymmetry in oxides: Hole doping in NiO versus electron doping in ZnO, *Phys. Rev. B* **75**, 241203 (2007).
- [57] A. Goyal and V. Stevanović, Metastable rocksalt ZnO is *p*-type dopable, *Phys. Rev. Mater.* **2**, 084603 (2018).
- [58] Y. Ogo, H. Hiramatsu, K. Nomura, H. Yanagi, T. Kamiya, M. Hirano, and H. Hosono, *p*-Channel thin-film transistor using *p*-type oxide semiconductor, SnO, *Appl. Phys. Lett.* **93**, 032113 (2008).
- [59] See the Supplemental Material at <http://link.aps.org/supplemental/10.1103/PhysRevApplied.19.034063> for an evaluation of the accuracy of the DD hybrid functional; screening results with different criteria; K-impurity energies in Na<sub>3</sub>AgO<sub>2</sub>; band structures of NaCuO, KCuO, and RbCuO; electron-localization function in K<sub>2</sub>Pb<sub>2</sub>O<sub>3</sub>; and band structures of Rb<sub>2</sub>Pb<sub>2</sub>O<sub>3</sub> and Cs<sub>2</sub>Pb<sub>2</sub>O<sub>3</sub>.
- [60] J. B. Varley, V. Lordi, A. Miglio, and G. Hautier, Electronic structure and defect properties of B<sub>6</sub>O from hybrid functional and many-body perturbation theory calculations: A possible ambipolar transparent conductor, *Phys. Rev. B* **90**, 045205 (2014).
- [61] H. Klassen and R. Hoppe, Alkalioxoargentate(I). Über Na<sub>3</sub>AgO<sub>2</sub>, *Z. Anorg. Allg. Chem.* **485**, 92 (1982).
- [62] K. Momma and F. Izumi, VESTA3 for three-dimensional visualization of crystal, volumetric and morphology data, *J. Appl. Crystallogr.* **44**, 1272 (2011).
- [63] K. Matsuzaki, N. Tsunoda, Y. Kumagai, Y. Tang, K. Nomura, F. Oba, and H. Hosono, Hole-doping to a Cu(I)-based semiconductor with an isovalent cation: Utilizing a complex defect as a shallow acceptor, *J. Am. Chem. Soc.* **144**, 16572 (2022).
- [64] H. Klassen and R. Hoppe, Neue Oxocuprate(I): Zur Kenntnis von CsCuO, *Z. Anorg. Allg. Chem.* **497**, 70 (1983).
- [65] R. D. Shannon, Revised effective ionic radii and systematic studies of interatomic distances in halides and chalcogenides, *Acta Crystallogr. A* **32**, 751 (1976).
- [66] B. Silvi and A. Savin, Classification of chemical bonds based on topological analysis of electron localization functions, *Nature* **371**, 683 (1994).
- [67] K-P Martens and R. Hoppe, Zum System K<sub>2</sub>O/PbO. Zur Kenntnis von K<sub>2</sub>Pb<sub>2</sub>O<sub>3</sub>, *Z. Anorg. Allg. Chem.* **437**, 116 (2010).
- [68] J. Shi, *et al.*, Modulation of the Bi<sup>3+</sup>6s<sup>2</sup> lone pair state in perovskites for high-mobility *p*-type oxide semiconductors, *Adv. Sci.* **9**, 2104141 (2022).
- [69] S. Chae, *et al.*, Toward the predictive discovery of ambipolarly dopable ultra-wide-band-gap semiconductors: The case of rutile GeO<sub>2</sub>, *Appl. Phys. Lett.* **118**, 260501 (2021).
- [70] S. Nakamura, N. Iwasa, M. S. M. Senoh, and T. M. T. Mukai, Hole compensation mechanism of *p*-type GaN films, *Jpn. J. Appl. Phys.* **31**, 1258 (1992).
- [71] Y. Kumagai, [https://github.com/yuukuma/p\\_tco\\_2023](https://github.com/yuukuma/p_tco_2023)